

1 **A LATE QUATERNARY RECORD OF SEASONAL SEA SURFACE TEMPERATURES OFF SOUTHERN**  
2 **AFRICA**

3 Loftus E<sup>a\*</sup>, Sealy J<sup>b</sup>, Leng MJ<sup>c, d</sup>, Lee-Thorp JA<sup>a</sup>

4 \*emma.loftus@rlaha.ox.ac.uk

5 <sup>a</sup> Research Laboratory for Archaeology and the History of Art, University of Oxford, Dyson Perrins  
6 Building, South Parks Road, Oxford, OX1 3QY, UK

7 <sup>b</sup> Department of Archaeology, University of Cape Town, Private Bag X3, Rondebosch 7701, South  
8 Africa

9 <sup>c</sup> NERC Isotope Geosciences Facilities, British Geological Survey, Keyworth, Nottingham NG12 5GG,  
10 UK

11 <sup>d</sup> Centre for Environmental Geochemistry, School of Geography, University of Nottingham,  
12 Nottingham NG7 2RD, UK

13

14 **ABSTRACT**

15 The southern Cape coastal region is important for understanding both the behavioural history of  
16 modern humans, and regional and global climate dynamics, because it boasts a long archaeological  
17 record and occupies a key geographical location near the intersection of two major oceans. The  
18 western boundary Agulhas Current, implicated in global heat exchange dynamics, is an important  
19 modulator of southern African climates and yet we understand its past behaviour only broadly as the  
20 Current itself scours the coastal shelf and marine sediment core records necessarily provide little  
21 detail. Numerous archaeological sites from both the late Pleistocene and Holocene provide the  
22 opportunity for reconstruction of near-shore seasonal SST records, which respond both to localized  
23 wind-driven upwellings and Agulhas temperature shifts, corresponding in turn with terrestrial  
24 precipitation trends in the near-coastal and summer rainfall regions. Here we present a record of  
25 seasonal SSTs extending over MIS5, MIS4, and the Holocene, from serial  $\delta^{18}\text{O}$  measurements of a  
26 single gastropod species, *Turbo sarmaticus*. The results show that mean SST shifts accord well with  
27 global SST trends, although they are larger than those recorded in the Agulhas Current from coarser-  
28 scale marine sediment records. Comparison with a record of Antarctic sea-ice suggests that annual  
29 SST amplitude responds to Antarctic sea-ice extent, reflecting the positioning of the regional wind  
30 systems that drive upwelling dynamics along the coast. Thus, near-shore SST seasonality reflects the  
31 relative dominance of the westerly and easterly wind systems. These data provide a new climate  
32 archive for an important but understudied climate system.

33 **Keywords:** Late Pleistocene; Holocene; palaeoclimatology; southern Africa; Agulhas Current; oxygen  
34 isotopes; mollusc shells; westerly winds

35 **Abbreviations**

36 AC – Agulhas Current; BNK1 – Byneskranskop1; HRC – Hoffman’s Robberg Cave; KRM –  
37 Klasies River Main site; NBC – Nelson Bay Cave; PP5-6 – Pinnacle Point 5-6; SST – sea surface  
38 temperature.

## 39 **1 Introduction**

40 The climate of southern Africa is strongly seasonal, with a summer-rainfall climate extending over  
41 much of the eastern and northern parts of the subcontinent, and grading into a Mediterranean-like,  
42 winter-rainfall climate in the south-west (see Figure 1; Tyson and Preston-Whyte, 2000). The southern  
43 Cape lies between these two dominant precipitation regimes and experiences a gradient of rainfall  
44 seasonality along its length, and is thus sensitive to shifts in the rain-bearing easterly and westerly  
45 wind systems. The coastline, a mixture of rocky and sandy shores subject to high-energy wave action,  
46 is adjacent to a large coastal plain, currently submerged but exposed to various degrees in the past  
47 depending on global sea levels (van Andel, 1989). Numerous late Pleistocene and Holocene  
48 archaeological sites along the coastline of the modern high-sea stand attest to the importance of this  
49 coastal shelf region for the history of modern humans.

50 The Agulhas Current (AC), with an estimated annual transport volume of *c.* 65 Sverdrup, is the largest  
51 western boundary current in the Southern Hemisphere (Lutjeharms, 2006), and forms part of the  
52 wind-driven circulation of warm tropical waters in the south Indian Ocean. The Current flows from  
53 approximately 25°S, along the South African coastal shelf to the southern tip of Africa, where it  
54 abruptly retroflects southwards and flows east as the Agulhas Return Current (see Figure 1). At the  
55 retroflection, large eddies and rings of warm, salty water occlude off and travel northwards into the  
56 South Atlantic Ocean. This leakage of warm Agulhas water into the Atlantic is an important process in  
57 the global redistribution of energy via the Atlantic Meridional Overturning Circulation (Beal et al.,  
58 2011). The AC is fed mostly by water from a South West Indian Ocean sub-gyre, which circulates in the  
59 Agulhas Basin. Some water is also fed in via the Mozambique Current and the East Madagascar Current  
60 in the form of intermittent eddies and rings, which contribute to a seasonal signal in the flow of the  
61 Agulhas Current (Lutjeharms, 2006).

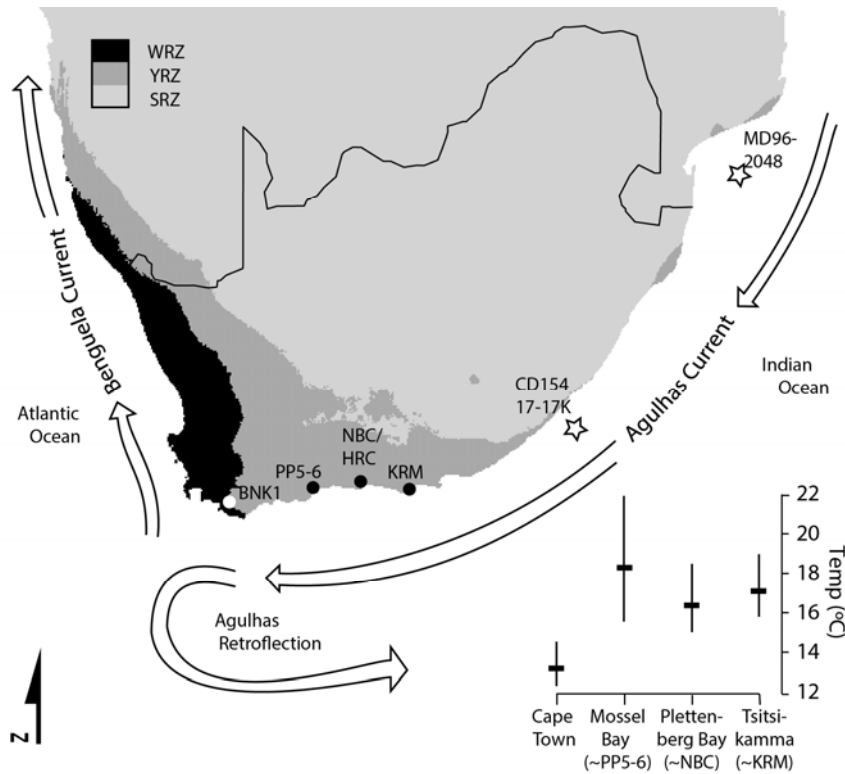
62 Cohen and Tyson (1995) presented a theoretical model to interpret near-shore sea surface  
63 temperature (SST) records along the southern cape, based on an understanding of the main influences  
64 on the regional climate and oceanic systems as reflected in marine mollusc records. According to the  
65 model, during periods of increased westerly winds, such as the austral winter when the circumpolar  
66 vortex is displaced equator-ward and westerly systems are forced northwards over the southern Cape  
67 (Cockcroft et al., 1987), the flow of the Agulhas is weakened and warm waters are advected onshore.  
68 At the same time, atmospheric circulation over the southwest Indian Ocean is also weakened and less  
69 warm, and moist air is advected over the subcontinent. Consequently, the model predicts that warm  
70 surface waters in the Agulhas system and near-shore zone are associated with dry conditions in the  
71 interior, summer rainfall zone ("dry-spell mode" – although note that the winter rainfall region will  
72 receive more rainfall from the northwards-shifted westerly systems). Conversely, during summer-like  
73 conditions when the zone of westerly winds is forced polewards, there is an increased frequency of  
74 alongshore easterly-component winds, and surface waters are advected away from the coast by  
75 Ekman transport processes. Cooler bottom waters upwell along the in-shore edge of the Agulhas  
76 Current, causing the thermocline to rise and leading to rapid drops in coastal SSTs that typically persist  
77 for several days (Schumann, 1999; Schumann et al., 1995). These easterly component winds advect  
78 warm, moist air over the eastern half of the subcontinent, and bring rainfall to this region.  
79 Consequently, the model predicts that cool surface waters along the southern coast during the  
80 summer are associated with wet conditions in the summer rainfall zone ("wet-spell mode"). Given the  
81 seasonal dimension of this mechanism, with summer SSTs primarily affected by the upwelling  
82 processes, shifts in seasonal amplitude can distinguish upwelling-driven SST fluctuations in the near-  
83 shore zone from global SST shifts due to glacial/interglacial dynamics. Cohen and Tyson (1995) also

84 produced a relatively modest dataset of Holocene SST estimates from oxygen isotope analyses of  
85 limpet shells preserved at Nelson Bay Cave (see Figure 1) and noted that this dataset seemed  
86 consistent with the model described above.

87 The behaviour of the AC over longer timescales is as yet only poorly understood, despite its important  
88 role in global and regional climates. This is in part due to the scarcity of long, finely-resolved archives,  
89 as the AC itself scours away much of the sediment from the coastal shelf. Even fewer records reveal  
90 details of seasonal conditions in the past, yet seasonality is an important dimension of regional  
91 climates, and structures much of the ecological patterning across the subcontinent. The best  
92 possibilities for records with the required temporal resolution and chronological control come from  
93 material within stratified archaeological sites. Serial oxygen isotope analysis of mollusc shell  
94 increments is one of the few proxies of palaeo-SSTs capable of providing robust measures of intra-  
95 annual SSTs outside of the tropics (e.g. Carré et al., 2005; Ferguson et al., 2011).

96 The oxygen isotope composition ( $\delta^{18}\text{O}$ ) of calcium carbonate shells reflects both seawater  
97 temperature and seawater  $\delta^{18}\text{O}$  during formation (Urey et al., 1951). Serial sampling of incremental  
98 growth layers supplies a record of shifts in marine conditions throughout the growth of the shell. In  
99 regions where there are no fluctuations in seawater  $\delta^{18}\text{O}$ , the sequence largely records SST shifts.  
100 Mollusc shells are a common component of archaeological sites along the south coast of South Africa,  
101 collected by foraging people for food and discarded as refuse that has gradually accumulated in  
102 rockshelter and cave deposits. Importantly, such assemblages span tens of thousands of years of  
103 occupation in the region, with the same species represented throughout at many sites. The shells are  
104 dated by association with the stratified archaeological deposits, which in many cases provides better  
105 chronological control than other types of climate archive.

106 In order to address the gap in our understanding of seasonal variability of Agulhas SSTs over the late  
107 Pleistocene and Holocene and the implications for coastal climates, we use archaeological *Turbo*  
108 *sarmaticus* shells from five sites located along the south coast (see Figure 1) to derive seasonally  
109 resolved records of near-shore SSTs across the last glacial cycle. Serial  $\delta^{18}\text{O}$  measurements across the  
110 *T. sarmaticus* operculum have been shown to reliably capture mean SST parameters, including the  
111 mean annual SST value and the mean annual SST amplitude (Galimberti et al., 2016). Contrasting mean  
112 annual SST estimates with the annual SST amplitude (or difference between average SSTs of warmest  
113 and coolest months) allows one to distinguish annual SST shifts driven by global climate changes (i.e.  
114 glacial/interglacial dynamics) and seasonal effects due to changes in the upwelling regime (described  
115 above). The SST record presented here partitions into three broad periods: the first spans much of  
116 Marine Isotope Stage (MIS) 5; the second spans the MIS5/4 transition and the final period spans the  
117 terminal Pleistocene and the entire Holocene. Thus, this dataset samples both glacial and interglacial  
118 conditions and two periods of global climatic transition, providing information about AC seasonal  
119 dynamics during large global climate fluctuations.



120

121 **Figure 1** Map of southernmost Africa, showing the locations of the five archaeological sites in this  
 122 study (filled circles). Also shown are the modern rainfall zones receiving most (> 66%) annual  
 123 precipitation in summer (SRZ) and winter (WRZ), and the year-round rainfall zone (YRZ). The major  
 124 currents are shown schematically, and the position of two off-shore cores is indicated (stars). The  
 125 plot in the right-hand corner shows the annual mean SSTs at locations along the coast, with the  
 126 mean annual SST amplitude (mean SST of warmest month – coolest month) indicated by the vertical  
 127 bar. All SST data 2000–2010 (morning measurements), except at Plettenberg Bay, where 1990–2000  
 128 only was available. Data is from the South African Weather Service ([www.weathersa.co.za/climate](http://www.weathersa.co.za/climate)).

129 **2 Material and Methods**

130 **2.1 Archaeological sites**

131 Samples were obtained from five archaeological sites that span c. 500 km of the southernmost coast  
 132 of South Africa. The distribution of the archaeological sites along the southernmost coast ensures that  
 133 the temperature records at each are differentially influenced by the oceanographic gradients along  
 134 this coast (see Figure 1). Samples are from the MIS1 and 2 levels at Nelson Bay Cave (NBC: Deacon,  
 135 1986), Hoffman’s/Robberg Cave (HRC: Kyriacou 2009) and Byneskranskop 1 (BNK1: Schweitzer and  
 136 Wilson 1982) and the MIS4 and MIS5 levels of Pinnacle Point 5-6 (PP5-6: Fisher et al., 2015) and Klasies  
 137 River main site (KRM: Deacon and Geleijnse, 1988; Wurz, 2002). NBC and HRC are located on the same  
 138 side of the Robberg Peninsula, about 800m apart, and reflect similar environmental conditions. These  
 139 sites are all caves or rock-shelters located at the modern coastline, except BNK1 which lies c. 10 km  
 140 inland. Deposits are mostly a series of human occupation layers interbedded with aeolian sands, and  
 141 each site contains well preserved organic material, including shells and faunal remains.

142 The sites were excavated over the last four decades and the shells used here were largely obtained  
 143 from museum collections – precise spatial information for each shell is available only at PP5-6, where  
 144 excavations are ongoing. Thus, samples were aggregated according to broad time periods or  
 145 depositional contexts defined by technological or sedimentological features (see Table 1). The  
 146 archaeological sequences of NBC and BNK1 span the terminal Pleistocene and Holocene (although

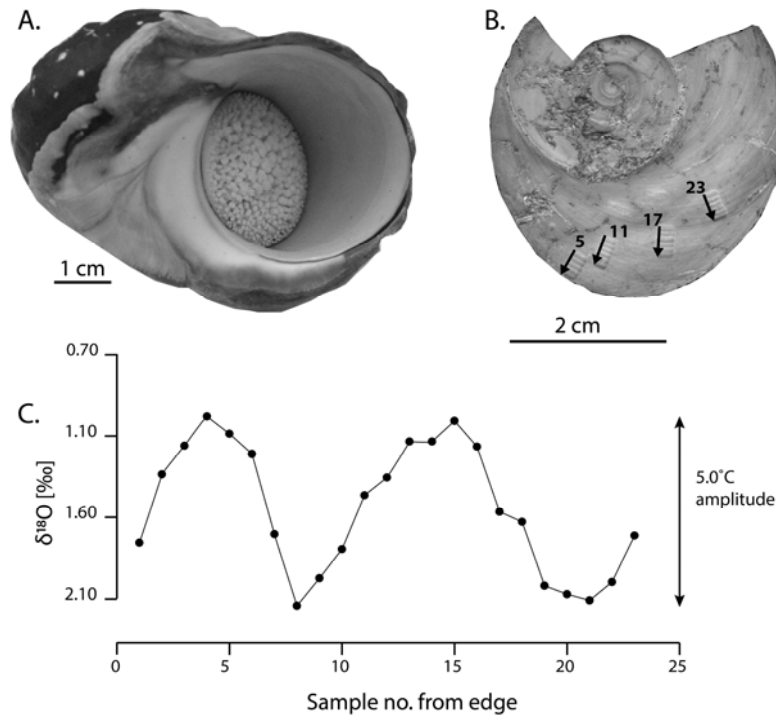
147 well-preserved shells are found only in the upper deposits at BNK1), and the chronologies of these  
148 two sites are securely underpinned by Bayesian modelled suites of conventional and accelerator  
149 radiocarbon dates (Loftus et al., 2016). The recent radiocarbon research at NBC has considerably  
150 improved the site's chronology since the study of Cohen and Tyson (1995). Radiocarbon dates from  
151 HRC show that the part of the sequence investigated thus far spans only a couple of thousand years  
152 in the late Holocene (Kyriacou, 2009). Samples from the three Holocene/ terminal Pleistocene sites  
153 are aggregated according to broad time divisions in the Holocene – early (c. 12-8 ka), middle (c. 8 – 4  
154 ka) and later (<4 ka), and the terminal Pleistocene (c. 12 – 14 ka). The KRM deposits are dated by a  
155 variety of methods (e.g. optically stimulated luminescence [OSL], electron-spin resonance and U-Th  
156 dating), but are constrained only very broadly to periods within MIS5 and samples are aggregated  
157 according to the technological units identified by Wurz (2002). The PP5-6 deposits, dated by OSL  
158 methods on sediments to periods within MIS5 and MIS4, are well constrained: samples are aggregated  
159 according to the depositional units, which are each dated to within a few thousand years (Karkanas et  
160 al., 2015).

## 161 **2.2 *Turbo sarmaticus* ecology and temperature record**

162 *Turbo sarmaticus* (or giant periwinkle, common name alikreukel) is a member of the globally  
163 distributed Turbinidae family known as turban shells, which are characterized by a hard, disc-like,  
164 aragonitic operculum that fits into the aperture of the topshell for protection from predators (see  
165 Figure 2A). A comparatively large macro-algal grazer endemic to the southern and eastern coasts of  
166 South Africa, *T. sarmaticus* is a common component of rocky shore communities along this coastline  
167 (Foster, 1997). The species inhabits the lower littoral (intertidal) and sublittoral regions to depths of  
168 approximately 8m (Branch et al., 2007). Typically, individuals occupy well-flushed locations and the  
169 high energy wave dynamics of this coastline ensure thorough water mixing.

170 One of the few studies of the life history of *T. sarmaticus* reports a growth rate among wild animals of  
171 approximately 25 mm/yr for the topshell and 9 mm/yr for the operculum during the first three years  
172 (Foster et al. 1999). The growth rate slows dramatically after this, to c. 5 mm/yr and 2 mm/yr for the  
173 topshell and operculum respectively. Animals can live up to 10 years (Bruton et al., 1991). The value  
174 of *T. sarmaticus* for palaeoenvironmental research derives from the robustness and good preservation  
175 of the operculum compared with other shells found in archaeological sites. *T. sarmaticus* opercula are  
176 frequently preserved largely intact, unlike thin-shelled topshells, bivalves and limpets, and form a  
177 significant component of south coast archaeological assemblages spanning the last glacial cycle (e.g.  
178 Langejans et al. 2012).

179 The *T. sarmaticus* operculum does however present challenges for seasonal-resolution sampling as  
180 many commonly used sclerochronological methods cannot be applied. The portion of the operculum  
181 with regular growth increments is just a few millimetres thick, so the operculum cannot be sectioned  
182 or polished prior to sampling and must be sampled directly from the ridged surface. Annual growth  
183 patterns are not clearly identifiable, and the growth of the opercula is slow relative to many species  
184 used in similar studies, limiting the number of samples per annual cycle and the possibility of using  
185 statistical curve-fitting approaches to reconstruct seasonality. Additionally, the direction of growth  
186 changes abruptly throughout life as the animal rotates the operculum to better fit the aperture of the  
187 coiling topshell during growth (see Figure 2).



188

189 **Figure 2 (A) *Turbo sarmaticus* shell with operculum pulled into aperture; (B) Inner surface of**  
 190 **broken archaeological *T. sarmaticus* operculum from PP5-6 (ID PP131492 from context SADBS, 71**  
 191  **$\pm$  3 ka) with 23 micromilled samples (numbered), arrows indicating the changing direction of**  
 192 **growth and sampling path; and (C)  $\delta^{18}\text{O}$  measurements of PP131492, showing the seasonal SST**  
 193 **signal, with the annual SST amplitude indicated.**

194 Notwithstanding the complexity of the growth patterns, earlier studies have indicated the utility of  
 195 this species for archaeological research and palaeotemperature reconstruction. Shackleton (1982)  
 196 analysed  $\delta^{18}\text{O}$  of a small number of opercula from KRM; his purpose was to establish a chronology for  
 197 the shell midden based on the global sea-level curve. Henshilwood (2008) measured archaeological *T.*  
 198 *sarmaticus*  $\delta^{18}\text{O}$  to explore changes in the seasonal timing of shellfish harvesting during the Holocene.  
 199 Most recently, Galimberti et al. (2016) undertook a systematic study of modern *T. sarmaticus*  
 200 opercula, collected from Mossel Bay between 2004-2007, to determine the reliability of temperature  
 201 records from this species. The data show that *T. sarmaticus* precipitate their shells in equilibrium with  
 202 water temperature and the Grossman and Ku (1986) palaeotemperature equation for all carbonates  
 203 (as modified by Hudson and Anderson (1989) to account for the 0.2‰ difference between SMOW and  
 204 average marine water) is most appropriate for this species:

205 
$$T (^{\circ}\text{C}) = 19.7 - 4.34 * (\delta^{18}\text{O}_{\text{aragonite}} - \delta^{18}\text{O}_{\text{water}}),$$

206 where the  $\delta^{18}\text{O}_{\text{water}}$  value is 0.52‰, as established by modern measurements at Mossel Bay  
 207 (Galimberti et al., 2016).

208 The modern data of Galimberti et al. (2016) show that although single individuals do not necessarily  
 209 capture the full annual temperature amplitude recorded by *in situ* thermometers, *mean* SST  
 210 parameters that represent typical conditions are accurately represented across a set of opercula.  
 211 Thus, the average shell-derived maximum (22.3°C) and minimum (15.6°C) SSTs match well with the  
 212 actual mean temperatures of the warmest and coolest months at Mossel Bay between 2000-2007 (Jan  
 213 = 22.4°C; Jul = 15.6°C). Consequently, the amplitude of SSTs from each shell averaged across the full

214 set of shells, 6.7°C, corresponds well with the average seasonal range of measured SSTs at Mossel Bay  
215 (6.8°C; i.e. the difference between the mean temperatures of the warmest and the coolest months).

216 Although it has been suggested that a truncated SST amplitude recorded in individual modern *T.*  
217 *sarmaticus* opercula might reflect physiological temperature limits for *T. sarmaticus* (i.e. temperatures  
218 above and below which they cannot grow), examination of archaeological data from an MIS5 site  
219 (Pinnacle Point 13b) suggests that this is not the case as these shells record cooler temperatures than  
220 the modern lower limit (data reported in a doctoral thesis; Galimberti, 2010). Additionally, the modern  
221 habitat of *T. sarmaticus* extends to the markedly cooler Atlantic waters around the Cape Point  
222 peninsula (annual average SST = 13.3°C; Branch et al., 2007). These observations suggest that the  
223 attenuated SST amplitude recorded in individual opercula might reflect either a physiological limit on  
224 time spent growing driven by their biological clocks, and that the animals can in fact shift their  
225 temperature tolerances to some degree, or rather that the sampling resolution of the Galimberti et  
226 al. (2016) study was simply inadequate to capture periods of slower growth during stressful growth  
227 seasons.

228 The approach taken here, where data from several archaeological opercula per context is aggregated  
229 to determine mean SST statistics, offers improved potential to capture the general environmental  
230 conditions compared with studies based on single shells per time unit, where microhabitat signals or  
231 stressful events in the life-histories of individual molluscs may introduce bias. Where climate is  
232 considered as the average state of environmental conditions aggregated over several decades,  
233 palaeoclimate records from high-resolution but short-lived archives such as mollusc shells require  
234 appropriately conservative interpretation.

### 235 **2.3 Shell selection and sampling**

236 *T. sarmaticus* precipitate their opercula as aragonite, a polymorph of CaCO<sub>3</sub> that is metastable under  
237 atmospheric conditions and is more vulnerable to dissolution and recrystallization than calcite, thus  
238 erasing the original oxygen isotope record in the process. Aragonitic shells provide an inherent  
239 advantage over calcitic shells for palaeoclimate reconstructions in that, while the potential for  
240 dissolution and recrystallisation is greater, the detection of calcite provides an unambiguous  
241 indication of recrystallization and altered shells can be removed from analysis. A greater challenge for  
242 this study is the patchy occurrence of diagenesis over the exposed surface of the opercula from which  
243 the growth increments are sampled. This variability of preservation within a single operculum  
244 demands a highly resolved assessment of recrystallization across the entire drilling path. In order to  
245 overcome this problem we applied a method based on Fourier transform infrared spectroscopy with  
246 an attenuated reflectance attachment (FTIR-ATR) to small aliquots (c. 0.5 mg) of powdered sample to  
247 test for and quantify the presence of calcite in several samples from each operculum (Loftus et al.,  
248 2015). Opercula were pre-screened using this method, whereupon approximately a quarter of the  
249 opercula were discarded, although this varied between the older, Pleistocene sites and the Holocene-  
250 aged sites where preservation was generally better. Upon micromill sampling, approximately every 4<sup>th</sup>  
251 or 5<sup>th</sup> milled sample (i.e. 2 - 3 mm) was screened with FTIR-ATR, and if recrystallisation was detected  
252 along the drilling path then the series of powdered samples continuing past the altered patch were  
253 discarded. Approximately a fifth of the milled samples from all sites were discarded in this way.

254

255 **Table 1 All sample contexts, correction for global changes in oceanic  $\delta^{18}\text{O}$  averaged across the age**  
 256 **range for each context (based on Waelbroeck et al., 2002), and the numbers of samples analysed.**  
 257 **Holocene sub-contexts from NBC, BNK1 or HRC are distinguished by the first letter N, B or H,**  
 258 **respectively. Calibrated radiocarbon dates for NBC and BNK1 in Loftus et al. (2016), and for HRC in**  
 259 **Kyriacou (2009). OSL ages for PP5-6 in Karkanis et al. (2015), KRM dated with various methods, see**  
 260 **Wurz (2002). Welch's unequal variances t-test results for significant differences between opercula**  
 261 **from the same sub-context are indicated (\*:  $p < 0.05$ ; \*\*:  $p < 0.001$ ; data were tested for normality).**

	Context	Sub-contexts	Date (ka)	$\delta^{18}\text{O}$ correction (‰)	No. of opercula	No. of $\delta^{18}\text{O}$ samples
NBC, HRC and BNK1		Sub-total			7	104
	Late Holocene < 4.2 ka	B_1_Eva	1.7-1.9	0	1	
		N_EIII	2.5	0	2	
		B_4_Dud	3.7-4.0	0	2	
		H_RR_P	4.0-4.3	0	2	
		Sub-total			9	159
	Mid Holocene c. 4.2 - 8.2 ka	B_5_Inge	3.9-6.1	0.03	1	
		N_Ivan**	4.9-6.6	0.03	2	
		B_6_Hilary	6.1-6.6	0.04	1	
		N_Glen	5.9-7.0	0.06	1	
		B_9_Mort**	6.4-7.4	0.06	2	
		Sub-total			8	165
	Early Holocene c. 8.2 - 11.9 ka	N_RiceB*	9.2-9.7	0.21	2	
		N_Jake	9.5-11.4	0.30	4	
		N_BSBJ**	10.9-11.9	0.48	2	
	End Pleistocene	N_GSL**	12.0 - 14.9	0.75	3	65
	PP5-6	DBCS	62 ± 3	0.54	1	20
OBS1		69 ± 3	0.64	5	80	
SADBS		71 ± 3	0.58	8	151	
ALBS		72 ± 3	0.51	5	74	
LBSR		81 ± 4	0.22	5	74	
KRM	MSA II Upper	c. 80 - 85	0.22	7	104	
	MSA II Lower	c. 90 - 95	0.32	8	112	
	MSA I	c. 115-120	0.07	6	67	
	Total			72	1175	

262

263 After pre-screening, opercula were micromilled using a New Wave Merchantek micromill with  
 264 tungsten carbide dental burrs (0.8 mm – overlapping of samples allows for c. 0.6 mm resolution).  
 265 Samples were taken in a nested series of curved lines that lie perpendicular to the direction of growth.  
 266 This sampling strategy is unlike previous sampling efforts: continuous, curving arcs of individual holes  
 267 that followed the mid-line of the operculum (Galimberti et al., 2016; Henshilwood, 2008; Shackleton,  
 268 1982). Rather, the direction of sampling is shifted in accordance with the direction of growth changes,  
 269 forming sets of discontinuous, but overlapping, samples (see Figure 2B). The number of analytical  
 270 samples per operculum ranges from 5 to 26, depending on size and preservation of the shell.



271 Twenty-seven opercula were sampled from the three Holocene sites (including the terminal  
 272 Pleistocene deposits at NBC), and 45 from the Late Pleistocene sites, 24 from PP5-6 and 21 from KRM  
 273 (see Table 1). Table 1 also shows the age for each context and sub-context where this can be resolved,  
 274 and the correction applied for changes in global ocean  $\delta^{18}\text{O}$  across the glacial cycle according to  
 275 Waelbroeck et al. (2002). The error of the correction is a result of the age uncertainty of the sample  
 276 in each case.

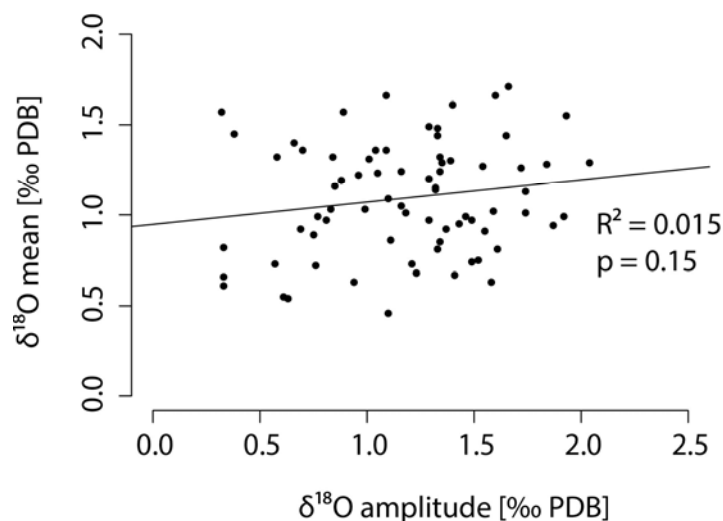
## 277 2.4 Analyses

278 Carbonate samples with < 10% calcite were analysed on one of three systems (indicated in Table SM1)  
 279 - a Kiel Device coupled to a Delta V Advantage isotope mass spectrometer in the Earth Science  
 280 Department, University of Oxford (external reproducibility of 0.10‰ for  $\delta^{18}\text{O}$ ); an automated Thermo  
 281 GasBench II device, coupled to a Thermo Delta V Advantage isotope mass spectrometer at the Division  
 282 of Archaeological, Geographical and Environmental Sciences of the University of Bradford (external  
 283 reproducibility of 0.30‰ for  $\delta^{18}\text{O}$ ); and a Multiprep device coupled to a GV Isoprime isotope mass  
 284 spectrometer at the NERC Isotope Geosciences Facilities at the British Geological Survey, Keyworth  
 285 (external reproducibility of <0.10‰ for  $\delta^{18}\text{O}$ ). In each case  $\text{CO}_2$  was produced by 100% phosphoric acid  
 286 hydrolysis, and the solid-gas fractionation of the samples is corrected using an aragonite specific factor  
 287 with appropriate corrections for reaction temperature (1.00906 at 71°C [Kiel and Gasbench], 1.00854  
 288 at 90°C [Isoprime]; Kim et al., 2007). For the calculation of temperatures from a carbonate  
 289 palaeotemperature equation (Grossman and Ku, 1986), however, the  $\delta^{18}\text{O}$  values are adjusted for  
 290 solid-gas fractionation using a calcite-specific factor (1.00868 at 71°C, 1.00813 at 90°C; Kim et al.,  
 291 2007) as the Grossman and Ku (1986) study did not take into account the differing fractionation factors  
 292 (see also Füllenbach et al., 2015) – accordingly, both sets of  $\delta^{18}\text{O}$  values are reported to aid comparison  
 293 between studies. The samples were calibrated against internal calcite standards calibrated in turn to  
 294 international standards (NBS19:  $\delta^{18}\text{O} = -2.20\text{‰}$ ). Results are reported in the delta-notation relative to  
 295 V-PDB, according to the equation:

$$296 \quad \delta^{18}\text{O} (\text{‰}) = \left\{ \left( \frac{R_{\text{SAMPLE}}}{R_{\text{STANDARD}}} \right) - 1 \right\} \times 1000,$$

297 where  $R_{\text{SAMPLE}}$  and  $R_{\text{STANDARD}}$  is the  $^{18}\text{O}/^{16}\text{O}$  ratio of the sample and reference materials.

298 **Figure 3 Scatterplot showing linear regression model of mean  $\delta^{18}\text{O}$  value for each shell against the**  
 299 **amplitude of  $\delta^{18}\text{O}$  values per shell.**



300

301 **Table 2** Summary statistics for *Turbo sarmaticus*  $\delta^{18}\text{O}$  data from all archaeological contexts (see  
302 supplementary table for data), with reconstructed temperatures using the Grossman and Ku (1986)  
303 equation for all data (as modified by Hudson and Anderson (1989)).  $\delta^{18}\text{O}$  values are shown adjusted  
304 for solid-gas fractionation using an aragonite specific factor, and a calcite factor for application in the  
305 palaeotemperature (PT) equation, (resulting in values c. 0.4‰ more positive). The  $\delta^{18}\text{O}_{\text{water}}$  value for  
306 the equation is 0.52‰, adjusted by the change in global ocean  $\delta^{18}\text{O}$  for each context, as recorded in  
307 Table 1. Also shown are the data from modern opercula collected by Galimberti et al. (2016) and the  
308 departures between the modern and archaeological data. The averaged parameters from each level  
309 are calculated from the maximum, minimum and amplitude of each operculum from that level (see  
310 section 2.2), and so cannot be calculated for DBCS at PP5-6, where only one operculum was available.

		Number of analyses	Number of shells	Mean	Ave. max $\delta^{18}\text{O}$ / Ave. min T(°C)	Ave. min $\delta^{18}\text{O}$ / Ave. max T(°C)	Ave. ampli- tude	
	Modern	$\delta^{18}\text{O}$ (‰)	327	16	+0.69	+1.47	-0.07	
		T(°C) conversion			19	15.6	22.3	6.7
	Late Holocene	$\delta^{18}\text{O}$ (‰)	104	7	+1.06	+1.56	+0.46	
		PT $\delta^{18}\text{O}$ (‰)			+1.44	+1.96	+0.85	
		T(°C) conversion			15.7	13.5	18.3	4.8
		T(°C) dep. from modern			-3.3	-2.1	-4.0	-1.9
	Mid Holocene	$\delta^{18}\text{O}$ (‰)	159	9	+1.27	+1.70	+0.73	
		PT $\delta^{18}\text{O}$ (‰)			+1.67	+2.09	+1.11	
		T(°C) conversion			14.7	12.9	17.1	4.2
		T(°C) dep. from modern			-4.3	-2.7	-5.1	-2.5
NBC, BNK1 and HRC	Early Holocene	$\delta^{18}\text{O}$ (‰)	165	8	+1.58	+2.16	+0.91	
		PT $\delta^{18}\text{O}$ (‰)			+1.96	+2.55	+1.29	
		T(°C) conversion			13.4	10.9	16.3	5.4
		T(°C) dep. from modern			-5.5	-4.7	-5.9	-1.2
	Late Pleistocene	$\delta^{18}\text{O}$ (‰)	65	3	+2.03	+2.78	+1.21	
		PT $\delta^{18}\text{O}$ (‰)			+2.38	+3.17	+1.60	
		T(°C) conversion			11.6	8.2	15.0	6.8
		T(°C) dep. from modern			-7.3	-7.4	-7.3	0.1
	DBCS	$\delta^{18}\text{O}$ (‰)	20	1	+1.48			
		PT $\delta^{18}\text{O}$ (‰)			+1.89	-	-	
		T(°C) conversion			13.8	-	-	-
		T(°C) dep. from modern			-5.2	-	-	-
	OBS1	$\delta^{18}\text{O}$ (‰)	80	5	+1.66	+2.38	+0.91	
		PT $\delta^{18}\text{O}$ (‰)			+2.07	+2.79	+1.32	
		T(°C) conversion			13.0	9.9	16.2	6.4
		T(°C) dep. from modern			-6.0	-5.7	-6.0	-0.3
PP5- 6	SADBS	$\delta^{18}\text{O}$ (‰)	151	8	+1.34	+1.99	+0.75	
		PT $\delta^{18}\text{O}$ (‰)			+1.75	+2.40	+1.16	
		T(°C) conversion			14.3	11.5	16.9	5.4
		T(°C) dep. from modern			-4.6	-4	-5.3	-1.3
	ALBS	$\delta^{18}\text{O}$ (‰)	74	5	+1.49	+1.81	+1.04	
		PT $\delta^{18}\text{O}$ (‰)			+1.90	+2.22	+1.45	
		T(°C) conversion			13.7	12.3	15.7	3.4
		T(°C) dep. from modern			-5.2	-3.3	-6.6	-3.3
	LBSR	$\delta^{18}\text{O}$ (‰)	74	5	+1.02	+1.53	+0.48	
		PT $\delta^{18}\text{O}$ (‰)			+1.43	+1.94	+0.89	
		T(°C) conversion			15.7	13.5	18.1	4.6
		T(°C) dep. from modern			-3.2	-2.1	-4.2	-2.1
KRM	MSAII upper	$\delta^{18}\text{O}$ (‰)	104	7	+1.57	+2.27	+0.91	
		PT $\delta^{18}\text{O}$ (‰)			+1.98	+2.68	+1.32	

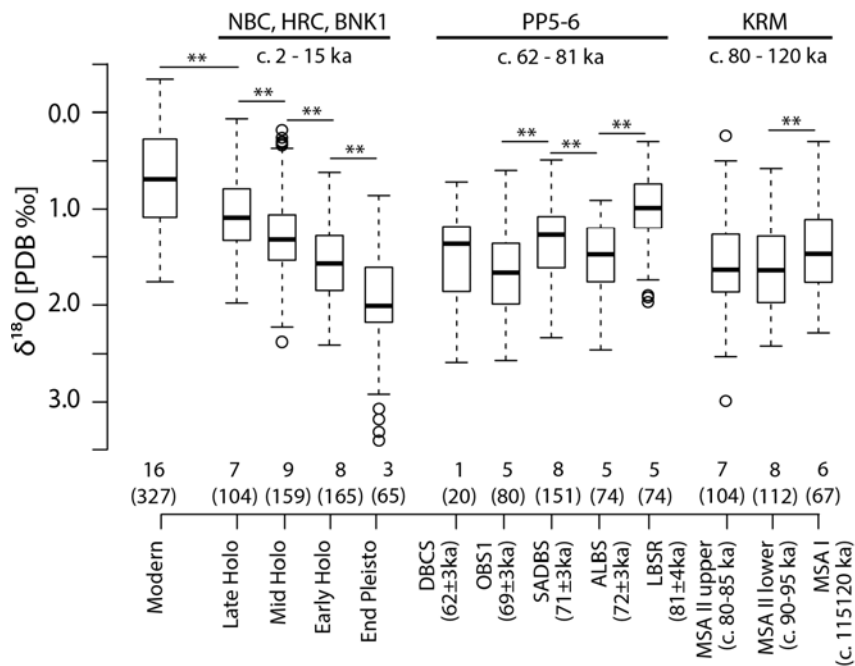
	T(°C) conversion			13.3	10.3	16.2	5.9
	T(°C) dep. from modern			-5.6	-5.3	-6.0	-0.8
MSAI lower	$\delta^{18}\text{O}$ (‰)	112	8	+1.60	+2.09	+0.96	
	PT $\delta^{18}\text{O}$ (‰)			+2.01	+2.50	+1.37	
	T(°C) conversion			13.2	11.1	16.0	4.9
	T(°C) dep. from modern			-5.7	-4.5	-6.2	-1.7
MSAI	$\delta^{18}\text{O}$ (‰)	67	6	+1.43	+1.88	+0.76	
	PT $\delta^{18}\text{O}$ (‰)			+1.84	+2.29	+1.17	
	T(°C) conversion			14.0	12.0	16.9	4.9
	T(°C) dep. from modern			-5.0	-3.6	-5.4	-1.8

311

### 312 3 Results

313 A total of 1175  $\delta^{18}\text{O}$  samples from 72 archaeological opercula were analysed (Table 1). The raw isotope  
 314 measurements, uncorrected for changes in global ocean  $\delta^{18}\text{O}$ , but corrected for solid-gas fractionation  
 315 using both aragonitic and calcitic (for palaeotemperature conversions) appropriate correction factors  
 316 are provided in supplementary material (Table SM1 and SM2). The serial isotope profiles of many  
 317 opercula produce seasonal cycles as expected (see Figures 2, SM1, SM2 and SM3). The key  $\delta^{18}\text{O}$  and  
 318 converted temperature statistics for each context are provided in Table 2. Figure 3 shows average  
 319  $\delta^{18}\text{O}$  values for each shell compared with the total  $\delta^{18}\text{O}$  amplitude for that shell using raw  $\delta^{18}\text{O}$  values.  
 320 The lack of a strong relationship (adjusted  $R^2 = 0.015$ ; p-value = 0.1494) between mean SST and SST  
 321 amplitude per shell supports the hypothesis that there is no bias against growth under cool climate  
 322 conditions and allows interpretation of changes in seasonal amplitude across the glacial cycle.

323 **Figure 4 Boxplots of *Turbo sarmaticus*  $\delta^{18}\text{O}$  values from each archaeological context (Table 2) with**  
 324 **sites indicated. Numbers of shells are shown below each box, with the number of analytical**  
 325 **samples in brackets. Note the left-hand scale has been reversed so that the top of the graph**  
 326 **reflects higher temperatures. Significant results for pairwise statistical comparisons are indicated**  
 327 **by \*\* (p<0.001; Post-hoc TukeyHSD test).**



328

329

### 330 **3.1 Glacial-interglacial shifts in near-shore seasonal SST record**

331 The aggregated  $\delta^{18}\text{O}$  measurements for each stratigraphic excavation unit are shown in Figure 3. The  
332 data show clear shifts in mean SST and annual SST amplitude. Across the terminal Pleistocene and  
333 Holocene, the shell-derived SSTs reflect a steady warming of  $4.1^\circ\text{C}$  (see also Figure 5), while a more  
334 variable pattern of SST change is recorded across the MIS5/4 transition, with SSTs declining by  $2.7^\circ\text{C}$   
335 overall from the oldest level at PP5-6, LBSR ( $82 \pm 4$  ka), to level OBS1 ( $82 \pm 3$  ka). At KRM, the SST  
336 record is considerably more stable, reflecting less than  $1^\circ\text{C}$  change across the three time periods.

337 The record also shows shifts in seasonality as recorded in the annual SST amplitude. During all three  
338 periods of the Holocene, mean minimum temperatures differ less from the modern dataset of  
339 Galimberti et al. (2016) than do the mean maximum temperatures. For example, during the late  
340 Holocene, the averaged minimum recorded SSTs are  $2.1^\circ\text{C}$  cooler than recorded by the modern  
341 dataset, but the averaged maximum recorded SSTs are  $4.0^\circ\text{C}$  cooler. This asymmetry in the departures  
342 between maximum and minimum temperatures suggests that during this period cooler summer SSTs  
343 had more of an effect on the overall temperature shifts than did the cooler winter SSTs. Arguably, this  
344 pattern of cooler maximum SSTs could simply reflect biased growth trends of *T. sarmaticus*, as the  
345 species might sufficiently slow its growth under cool conditions so that winter SST values are  
346 underrepresented. However, this interpretation is directly challenged by the data from the terminal  
347 Pleistocene levels, where the departure from modern was approximately equal (c.  $7.3^\circ\text{C}$ ) in the  
348 averaged maximum and minimum SSTs, indicating that at this time the cooling was more or less  
349 equally distributed throughout the year.

350 Figure 7(F) shows the annual average SST amplitude across all the data, which, for the terminal  
351 Pleistocene/Holocene dataset, is lowest during the mid-Holocene ( $4.2^\circ\text{C}$ ) and highest during the  
352 terminal Pleistocene ( $6.8^\circ\text{C}$ ). The situation is mirrored for the MIS5/4 data from PP5-6, where the  
353 annual SST amplitude is high in the glacial MIS4 assemblage in context OBS1 ( $69 \pm 3$  ka:  $6.4^\circ\text{C}$ ) and  
354 lower during the interglacial MIS5 assemblages in contexts LBSR ( $81 \pm 4$  ka:  $4.6^\circ\text{C}$ ) and ALBS ( $72 \pm 3$  ka:  
355  $3.4^\circ\text{C}$ ) especially (date ranges in Karkanis et al., 2015). Similar to the Holocene dataset, the low annual  
356 amplitudes in the PP5-6 dataset are driven by cooler maximum temperatures during both LBSR and  
357 ALBS, which are depressed by approximately twice as much as the minimum temperatures compared  
358 with modern values. During early MIS4 glacial OBS1, SSTs are depressed by c.  $5.7 - 6.0^\circ\text{C}$  year round,  
359 which is similar to the SST depression observed during the terminal Pleistocene.

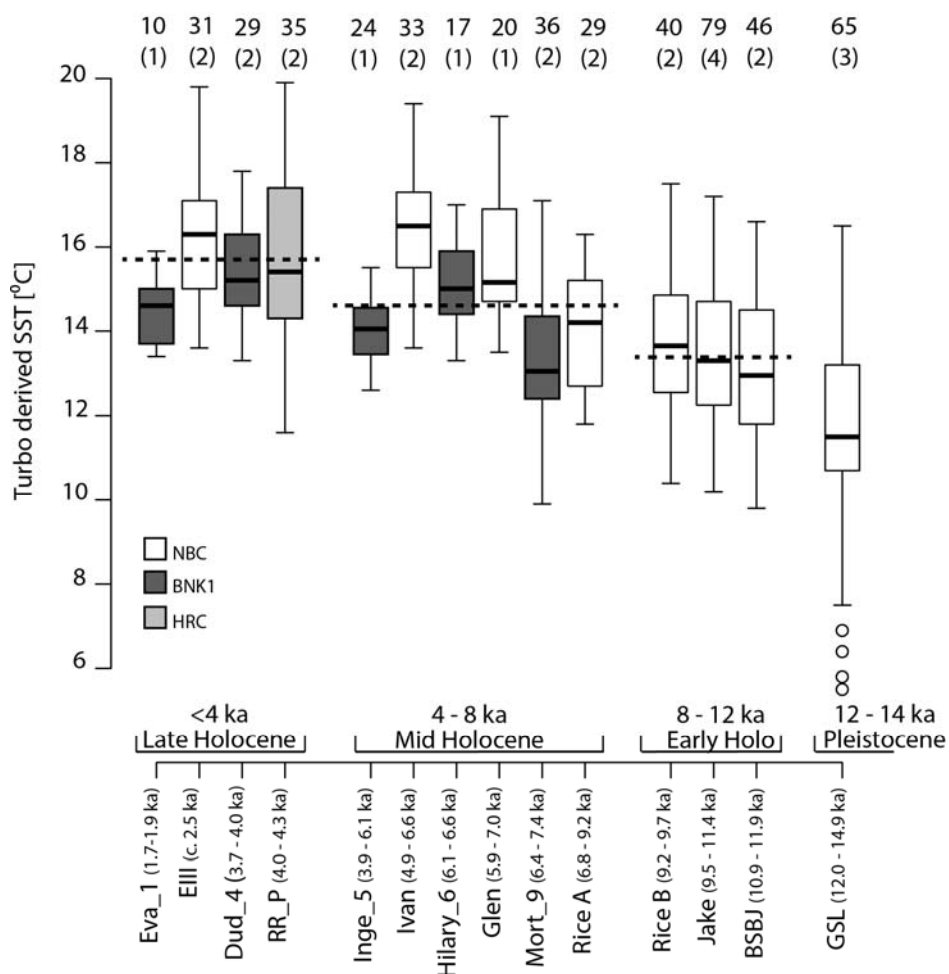
### 360 **3.2 Intra-context variability**

361 Chronological control among the Holocene-aged samples is sufficient to permit  $\delta^{18}\text{O}$  correction  
362 according to the age of the sub-context (see Table 1), allowing exploration of variability in SST  
363 estimates at finer timescales. More than one shell was measured from a single stratigraphic  
364 excavation unit or sub-context in ten instances (see Table 1), and significant differences are observed  
365 in five cases (with Welch two sample t-test for unequal sample sizes: significant results indicated in  
366 Table 1). These differences may reflect climatic changes occurring within the timespan represented  
367 by the stratigraphic sub-context or micro-scale differences in the habitats of individual *T. sarmaticus*.  
368 It is worth noting that only in one of these ten sub-contexts, where age estimates can span thousands  
369 of years, does the standard deviation among  $\delta^{18}\text{O}$  analyses exceed that recorded among all sixteen  
370 modern shells collected over just a few years ( $0.52\text{‰}$ , versus that of  $0.56\text{‰}$  during the terminal  
371 Pleistocene), and where the standard deviation presumably results from small differences in annual  
372 SSTs and microhabitat. Where two or more shells from a single depositional unit reflect similar mean  
373 temperatures, one can infer with greater confidence that the shells record average environmental  
374 parameters rather than microhabitat conditions. Yet, as demonstrated by the modern study of

375 Galimberti et al. (2016), analysis of multiple shells allows for more accurate reconstruction of  
 376 parameters such as mean SST and seasonal amplitude.

377 Figure 5 shows the shell-derived SSTs for the Holocene and terminal Pleistocene dataset, according to  
 378 sub-context. The same overall trends are evident as in Figure 4, although the magnitude of SST shifts  
 379 within each context are now clear. For example, during the mid-Holocene, SSTs at NBC fluctuate by  
 380 over 2°C from sub-context Rice A (14.0°C; 6.8-9.2 kcalBP, n=29) to Ivan (16.4°C; 4.9-6.6 kcalBP, n=33),  
 381 whereas SSTs change less than 1°C across the early Holocene from sub-context BSBJ (13.1°C; 10.9-11.9  
 382 kcalBP, n=46) to Rice B (13.7°C; 9.2-9.7 kcalBP, n=40), suggesting that the mid-Holocene witnessed  
 383 more dynamic conditions in the near-shore zone that did the early Holocene. Similar assessments of  
 384 intra-context variability will be possible further back in time at KRM and PP5-6, as ongoing dating  
 385 efforts at these sites improve the age estimates for the depositional contexts and allow for more  
 386 precise and accurate corrections for changes in ocean  $\delta^{18}\text{O}$ .

387 **Figure 5 Boxplots of *Turbo sarmaticus* shell  $\delta^{18}\text{O}$  derived temperatures by sub-unit and site for**  
 388 **Holocene and terminal Pleistocene aged samples (see Table 1 for contextual information). Dotted**  
 389 **horizontal lines indicate average temperature for the entire period. Number of analytical samples**  
 390 **and number of shells (in brackets) per unit is shown above each unit. Temperatures calculated**  
 391 **using the Grossman and Ku (1986) equation for all carbonates, as modified by Hudson and**  
 392 **Anderson (1989).**



393

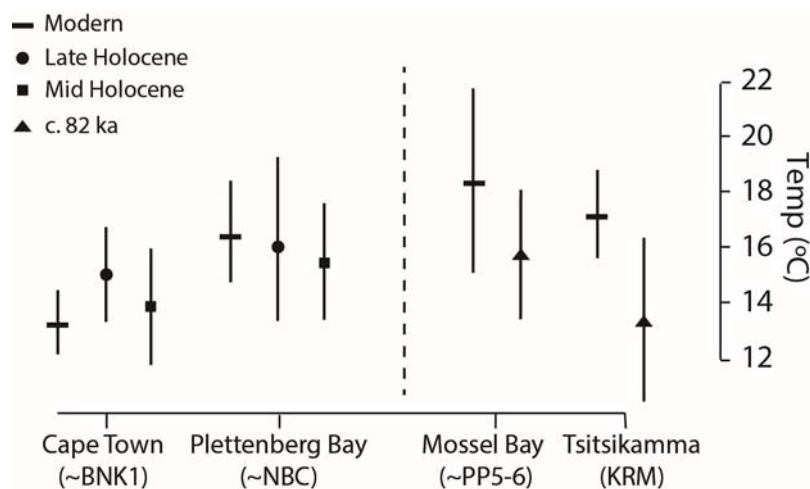
### 394 3.3 Spatial variation in near-shore SSTs

395 Along-shore SST trends can be reconstructed for the mid-late Holocene and at c. 82 ka, as data from  
 396 two geographically separated sites overlaps during these intervals. In the mid and late Holocene, shell-

397 derived SSTs from the Robberg Peninsula (NBC and HRC) are consistently higher than those from  
 398 BNK1, consistent with modern SST gradients between Plettenberg Bay (see Figure 6: instrumental  
 399 mean SST = 16.4°C; annual range = 3.6°C) and Cape Town, to the west of BNK1 (instrumental mean  
 400 SST = 13.3°C; annual range = 2.3°C; data available on request from South African Weather Service).  
 401 During the mid-Holocene, reconstructed mean annual SSTs at BNK1 are 13.9°C and on the Robberg  
 402 Peninsula 15.4°C; the average amplitude at both locations is the same (4.2°C). During the late  
 403 Holocene, the mean annual SST at BNK1 is 15.1°C, while that at Robberg is 16.0°C. The average  
 404 amplitude differs sharply between BNK1 (3.4°C) and the Robberg Peninsula (5.9°C).

405 At c. 82 ka, SSTs at KRM are 13.3°C, while those at PP5-6 are 15.7°C. This, too, is consistent with the  
 406 modern SST gradient, as instrumental temperatures recorded at Tsitsikamma, near to KRM, today  
 407 average 17.1°C, while those at Mossel Bay average 18.4°C. However, the average amplitude is only  
 408 4.6°C in level LBSR at PP5-6, while it is 5.9°C in the MSA II upper level at KRM. To contrast, the modern  
 409 annual SST range at Mossel Bay is 6.7°C and that at the Tsitsikamma SST station is 3.1°C. The large SST  
 410 range at Mossel Bay today is driven largely by very warm summer SSTs: conversely, the high SST  
 411 amplitude at KRM at 82 ka appears to be largely a result of very low winter SSTs, averaging 10.3°C at  
 412 this time.

413 **Figure 6 Mean shell-derived SST values by location along the south coast and by time period, with**  
 414 **modern SSTs (*in-situ* measurements available on request from South African Weather Service).**  
 415 **The mean annual temperature amplitude (i.e. difference between averaged maximum and**  
 416 **minimum temperatures) for each dataset is indicated by the vertical lines.**



417

## 418 4 Discussion

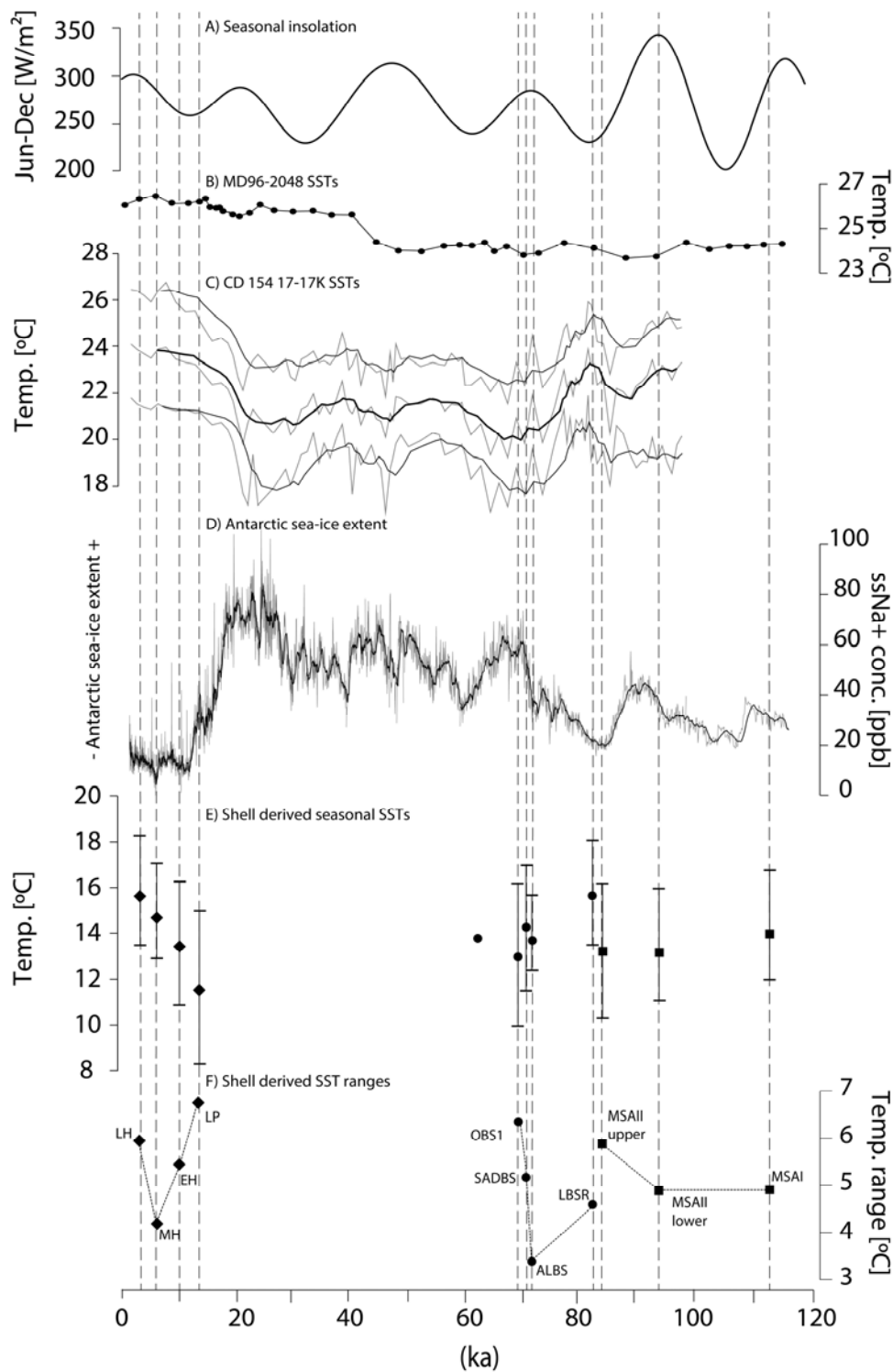
### 419 4.1 Agulhas Current and near-shore SST trends

420 The spatial patterns between the sites and the temporal shifts in temperature match well with both  
 421 the modern spatial temperature gradient along this coastline, and global climate shifts across MIS5  
 422 through the late Holocene, although our data represent but a small number of annual seasonal cycles  
 423 across each depositional unit. The clearest SST trend is the steady rise in temperatures from the  
 424 terminal Pleistocene through the Holocene. The PP5-6 data shows a gradual decline in temperatures  
 425 between 82 ± 4 ka (LBSR) and 69 ± 3 ka (OBS1), although the trend is not linear, suggesting that  
 426 fluctuations in local SST and oceanographic conditions accompanied the transition from interglacial to  
 427 glacial conditions between MIS5 and MIS4. In contrast, the MIS5 dataset from KRM shows relatively

428 little change between the three levels. This stability might indicate that the site was occupied only  
429 during MIS5 interstadials, which is consistent with the broad dates for the deposits.

430 Figure 7 shows a measure of regional climate seasonality (the difference between June and December  
431 insolation; Berger and Loutre, 1991), alongside a stacked record of AC SSTs for the last 115 ka from  
432 marine sediment core MD96-2048, located in the formation region of the AC adjacent to the Delagoa  
433 Bight (Caley et al., 2011); and a record of AC SSTs for the last 100 ka derived from marine sediment  
434 core CD154 17-17K located in the main trajectory of the AC (Simon et al., 2013). The SST estimates by  
435 Simon et al. (2013) are derived via a similarity index transfer function based on modern analogue  
436 foraminiferal assemblages, which allows for the estimation of summer and winter SSTs in addition to  
437 an annual average. Both the MD96-2048 and CD154 17-17K temperature estimates are for off-shore  
438 locations closer to the Indian Ocean, and so are not directly comparable with the shell-derived records  
439 of this study, which, in addition to responding to the SST shifts of the larger AC system, are also  
440 influenced by near-shore processes such as upwelling. These core records, however, provide  
441 information about the long-term behaviour of the Agulhas system (Caley et al., 2011), and their  
442 juxtaposition with the shell-derived SST records allows us to discern global and regional processes.  
443 Also shown in Figure 7 is an Antarctic record of sea salt sodium concentrations, a measure of polar  
444 sea-ice extent, which effects the position of the hemispheric wind belts (Fischer et al., 2007). These  
445 measures of seasonality, Agulhas Current conditions and hemisphere-wide atmospheric dynamics are  
446 displayed alongside the shell-derived mean SST reconstructions (mean, maximum and minimum per  
447 context) and shell-derived SST amplitudes (see Table 2).

448 Figure 7 Shell-derived SSTs by depositional unit against: A) insolation seasonality (June-December  
 449 insolation) at 30°S (Berger and Loutre, 1991); B) AC SSTs derived from Mg/Ca ratios and alkenone  
 450 and tetraether indices from marine core MD96-2048 (26° 10.0'S, 34° 1.0'E; Caley et al., 2011); C)  
 451 planktic foraminifera derived AC seasonal SSTs from marine sediment core CD154 17-17K (33°  
 452 19.2'S, 29° 28.2'E; Simon et al., 2013) with five point running averages overlaid, and D) sea salt  
 453 sodium concentrations from EPICA DML ice-core as a measure of sea ice extent (Fischer et al.,  
 454 2007). E) Shell-derived SSTs are shown with average maximum and minimum values and the F)  
 455 range between these values is plotted below. Robberg sites (NBC and HRC only: BNK1 values not  
 456 included here): diamonds; PP5-6: circles; and KRM: squares. Note that the data from PP5-6 unit  
 457 DBCS are not shown as they derive from only a single shell.





459 Neither the shell-derived average SSTs nor the annual SST amplitudes correspond with seasonal  
460 insolation, suggesting that other mechanisms drive the large shifts in SST and seasonality in the  
461 Agulhas and near-shore zone. While reconstructions of AC SSTs from offshore cores are considerably  
462 warmer than those reflected in the shell records, the magnitude of SST shifts is muted in the main  
463 Agulhas system compared with the near-shore zone (SSTs are displayed at the same scale in Figure 5).  
464 Moreover, the fluctuations in seasonal temperature amplitudes reported by Simon et al. (2013) are  
465 more constrained (between 4.0 - 5.6°C) compared to those from shell records (3.4 - 6.8°C), suggesting  
466 that seasonal amplitude in the main AC may be buffered from the processes that influence SST shifts  
467 and seasonal amplitude in the near-shore SST record. Admittedly, the marine core records are likely  
468 to be time averaged from mixing and bioturbation processes, dampening any large changes in annual  
469 SST.

470 The seasonal amplitude of nearshore SSTs corresponds well with a record of sea-ice extent from  
471 Antarctica (Fischer et al., 2007). During the terminal Pleistocene, when sea-ice was more extensive  
472 than during the Holocene, the larger seasonal amplitude of near-shore SSTs indicates summer  
473 upwelling was reduced. As sea-ice extent is known to affect the position of the dominant wind systems  
474 around southern Africa (Chase et al., 2015), this relationship suggests that the south coast experienced  
475 reduced frequency of the easterly winds that drive summer upwelling of cooler, deeper water, as the  
476 austral westerly wind systems were forced equatorwards over the southern part of South Africa.  
477 Conversely, during the mid-Holocene, the low amplitude of the near-shore SST reconstructions argues  
478 for enhanced summer upwelling, when sea-ice extent in the Atlantic sector of the Southern Ocean is  
479 most diminished (Fischer et al., 2007). Sea-ice extent around Antarctica subsequently expanded about  
480 5 ka through the late Holocene (Fischer et al., 2007), when the higher late Holocene shell-derived SST  
481 annual amplitude again indicates reduced summer upwelling and an increased influence of westerly  
482 winds.

483 A similar pattern is observed in the trend of SST amplitudes over the MIS5/4 transition. Increasing sea-  
484 ice extent across the transition is accompanied by increasing annual SST amplitudes in the near-shore  
485 SST reconstructions at PP5-6. During levels LBSR ( $82 \pm 4$  ka) and ALBS ( $72 \pm 3$  ka) at PP5-6, annual SST  
486 amplitudes were lower than in the subsequent SADB5 ( $71 \pm 3$  ka) and OBS1 ( $69 \pm 3$  ka) levels,  
487 suggesting a decrease in summer upwelling and an increased importance of westerly winds along the  
488 south coast, driven by expanded Antarctic sea-ice. However, the same pattern does not appear to  
489 hold in the MIS5 assemblages from KRM. While the two earliest assemblages (MSA I [115-120 ka] and  
490 MSA II lower [90 – 95 ka]) have equivalent annual SST amplitudes, the annual SST amplitude of MSA II  
491 upper (80 - 85 ka) is higher, suggesting a decrease in summer upwelling, yet sea-ice extent declines  
492 slightly across this period. However, the age ranges for the KRM deposits are not as well established  
493 as those of the other sites here – it is possible that ongoing dating studies at KRM will provide more  
494 precise and accurate age estimates for the deposits.

#### 495 **4.2 Near-shore SSTs and terrestrial precipitation trends**

496 According to the Cohen and Tyson (1995) model, shifts in near-shore SST seasonality respond to  
497 seasonal, wind-driven upwelling (e.g. decreased seasonality as a result of decreased summer SSTs  
498 linked to wind-driven upwelling). The low annual SST amplitude during the mid-Holocene indicates  
499 that upwelling intensity was greatest during the mid-Holocene, which would correspond with  
500 increased summer rainfall. Environmental records from the summer rainfall region show that the mid-  
501 Holocene was indeed a time of generally moister conditions (Scott et al., 2012; Scott and Lee-Thorp,  
502 2004). Warmer, moister conditions in the northern savanna region are reflected in the Makapansgat  
503 T7 speleothem between 6.4 – 5.1 ka (Holmgren et al., 2003; Lee-Thorp et al., 2001), and high water

504 levels are recorded in pans to the south, in the highveld grassland around Florisbad (Scott and Nyakale,  
505 2002). Pollen records from the coastal Lake Eteza, at the eastern edge of the subcontinent, capture a  
506 moist episode between c. 7 – 4 ka, which Scott et al. (2012) hypothesise is linked to the warming of  
507 the Agulhas: instead, we suggest here that it reflects increased easterly winds that are also recorded  
508 in the seasonal SST record of upwelling.

509 In contrast, during the terminal Pleistocene Younger Dryas event from c. 13 – 11.5 ka, generally dry  
510 conditions prevailed across the southern African interior (Scott et al., 2012), and this is consistent with  
511 the SST record of increased seasonality which suggests a low frequency of summer upwelling and  
512 easterly component winds at this time. Similarly, Scott et al. (2012) note lower moisture levels  
513 recorded in pollen records from several sites in the SRZ during the late Holocene, c. 3.5 - 1.5 ka, which  
514 is also suggested by the rise in seasonality seen in the late Holocene shell SST record. The Holocene  
515 SST record thus aligns well with the expectations of the Cohen and Tyson (1995) model for the SRZ.

516 Detailed records of SRZ precipitation are scarce for earlier periods, but the similarity between the  
517 pattern of increasing SST amplitude recorded across the MIS5/4 transition with the mirrored trend for  
518 the terminal Pleistocene/Holocene, suggests a decrease in summer rainfall in the interior across the  
519 MIS5/4 transition. One of the few archives that spans this period, the Tswaing crater sedimentary  
520 record (Partridge et al., 1997) shows a decrease in summer rainfall between MIS5/4. An off-shore  
521 record of terrestrial run-off, situated off the east coast of South Africa, shows spikes in summer rainfall  
522 during late MIS5 (Ziegler et al., 2013). However, the nature of that record is such that it does not  
523 capture periods of increased aridity.

524 An indirect line of evidence for drying in the SRZ during MIS4 comes from off-shore records along the  
525 western coast that show increasing proportions of rainfall in the WRZ, particularly from c. 73 – 57 ka  
526 (Chase, 2010). An increase in winter rainfall would result if the westerly wind system was forced  
527 northwards, which is consistent with the increased seasonality seen in the shell SST record. A  
528 confounding factor for reconstructing precipitation from terrestrial archives is the effect of global  
529 temperature shifts on aridity across this time – although summer rainfall may have decreased during  
530 MIS4, the year-round rainfall region remained generally humid due to the cooler temperatures and  
531 larger amounts of winter rainfall (Chase, 2010; Chevalier and Chase, 2016).

## 532 **5 Conclusions**

533 Seasonal near-shore SSTs as reconstructed from serial  $\delta^{18}\text{O}$  measurements of *Turbo sarmaticus*  
534 opercula collected from archaeological sites along the southernmost coast of South Africa correspond  
535 closely with global SST trends across MIS5, MIS4, the terminal Pleistocene and the Holocene. Largely  
536 stable SSTs across the interstadial periods of MIS5 are followed by sudden fluctuations in average SST  
537 across the MIS5/4 transition. From the terminal Pleistocene, average SSTs rise steadily through to the  
538 late Holocene, by a total of c. 4°C.

539 While seasonal insolation does not appear to correspond with the seasonality of near-shore SSTs,  
540 shifts in the annual SST amplitude may reflect wind-driven upwelling intensity, apparently in response  
541 to Antarctic sea-ice forcing of the westerly wind belt. Increased upwelling (as reflected in a low annual  
542 SST amplitude) during the mid-Holocene corresponds with increased precipitation in the summer  
543 rainfall region. Both increased upwelling intensity and summer precipitation amounts are predicted  
544 responses to an increased frequency of easterly component winds which bring moisture from the  
545 warm Agulhas and Indian Ocean. Conversely, reduced near-shore upwelling during the terminal  
546 Pleistocene (as reflected in a high annual SST amplitude), when sea-ice was more extensive and the

547 westerly wind systems were shifted equatorwards, corresponds with drier conditions over the  
548 summer rainfall zone. Similar, but mirrored, SST trends are observed across the MIS5/4 transition, in  
549 the PP5-6 assemblage. Increasing annual SST amplitude across the transition suggests a decrease in  
550 summer upwelling as sea-ice expanded around Antarctica. Such an expansion would force the  
551 westerly wind belt north, reducing the frequency of easterly component winds over the south coast  
552 and resulting in reductions in summer rainfall from MIS5 through to the start of MIS4.

553 This study augments the range of seasonal climate archives from a globally-important but poorly-  
554 understood system. More broadly, the approach taken here demonstrates the value of seasonally  
555 resolved near-shore SST records from archaeological marine molluscs for connecting marine and  
556 terrestrial climate systems. Oceanographic processes that primarily affect near-shore contexts should  
557 be distinguished from trends in the open ocean, as SST records from the two contexts are not  
558 equivalent. In this study, we link near-shore upwelling dynamics, as revealed in seasonal SST records,  
559 with regional precipitation trends, via latitudinal shifts in the rain-bearing wind systems (Cockcroft et  
560 al., 1987; Cohen and Tyson, 1995). Currently, the number of annual seasonal SST cycles represented  
561 in each depositional context is small for the purpose of defining average climate states, but given the  
562 large numbers of archaeological sites with well-preserved shell material along the South African  
563 coastline, the approach taken here offers good possibilities for developing detailed records of SST and  
564 precipitation shifts across the last glacial period for this region.

#### 565 **Acknowledgments**

566 This work was supported by the South African Research Chairs Initiative of the Department of Science  
567 and Technology and the National Research Foundation of South Africa; Merton College, Oxford; a  
568 Quaternary Research Association New Research Worker's Award, the Palaeontological Scientific Trust  
569 and a NERC Isotopes Geosciences Facilities Steering Committee Award (grant number IP-1543-0515).  
570 Permissions for export and sampling were obtained from the curator of the archaeological collections  
571 at Iziko Museum, Heritage Western Cape (case number 14072110GT0730E) and the Eastern Cape  
572 Provincial Heritage Resources Agency (permit number 2/2/APM-PERMIT/14/09/003). Grateful  
573 acknowledgments to Curtis Marean and Sarah Wurz for help accessing the collections from PP5-6 and  
574 KRM. Thanks are also due to Gideon Henderson for access to sampling equipment in the Department  
575 of Earth Sciences, Oxford and especially to Chris Day, Peter Ditchfield, Hilary Sloane, Chris Richardson  
576 and Andy Gledhill for help with analyses.

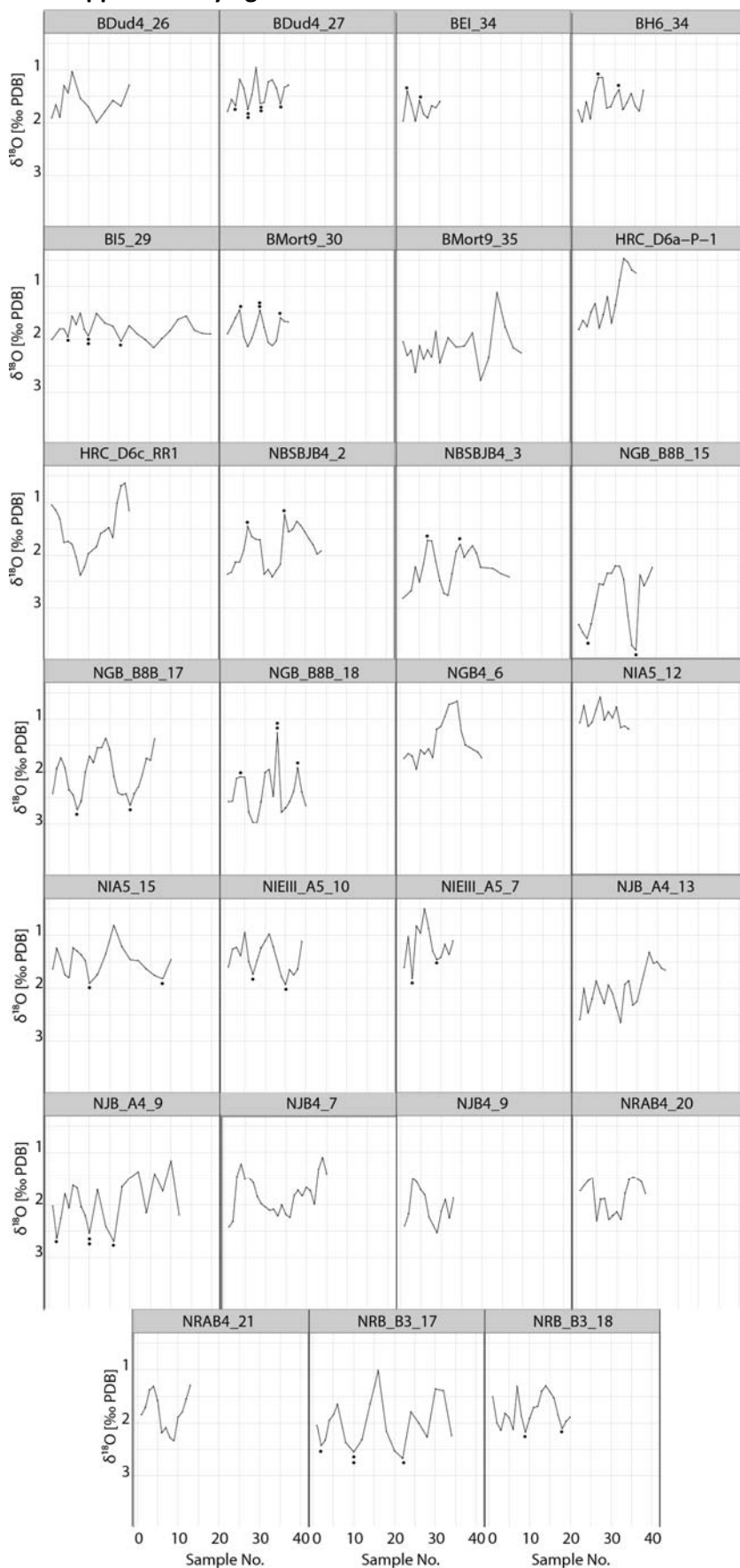
577 **6 References**

- 578 Berger, A., Loutre, M.F., 1991. Insolation values for the climate of the last 10 million years. *Quat. Sci.*  
579 *Rev.* 10, 297–317. doi:10.1016/0277-3791(91)90033-Q
- 580 Branch, G., Griffiths, C., Branch, M., Beckley, L., 2007. *Two oceans: a guide to the marine life of*  
581 *southern Africa*, 2nd ed. Struik Publishers, Cape Town.
- 582 Bruton, J., Baird, D., Coetzee, P.S., 1991. Population structure and yield-per-recruit analysis of the  
583 giant periwinkle *Turbo sarmaticus* in the Cape St Francis region, South Africa. *South African J.*  
584 *Mar. Sci.* 11, 345–356. doi:10.2989/025776191784287754
- 585 Caley, T., Kim, J.-H., Malaizé, B., Giraudeau, J., Laepple, T., Caillon, N., Charlier, K., Rebaubier, H.,  
586 Rossignol, L., Castañeda, I.S., Schouten, S., Sinninghe Damsté, J.S., 2011. High-latitude obliquity  
587 as a dominant forcing in the Agulhas current system. *Clim. Past* 7, 1285–1296. doi:10.5194/cp-  
588 7-1285-2011
- 589 Carré, M., Bentaleb, I., Fontugne, M., Lavalée, D., 2005. Strong El Niño events during the early  
590 Holocene: stable isotope evidence from Peruvian sea shells. *The Holocene* 15, 42.  
591 doi:10.1191/0959683605h1782rp
- 592 Chase, B.M., 2010. South African palaeoenvironments during marine oxygen isotope stage 4: a  
593 context for the Howiesons Poort and Still Bay industries. *J. Archaeol. Sci.* 37, 1359–1366.  
594 doi:10.1016/j.jas.2009.12.040
- 595 Chase, B.M., Lim, S., Chevalier, M., Boom, A., Carr, A.S., Meadows, M.E., Reimer, P.J., 2015. Influence  
596 of tropical easterlies in southern Africa’s winter rainfall zone during the Holocene. *Quat. Sci.*  
597 *Rev.* 107, 138–148. doi:10.1016/j.quascirev.2014.10.011
- 598 Chevalier, M., Chase, B.M., 2016. Determining the drivers of long-term aridity variability: a southern  
599 African case study. *J. Quat. Sci.* 31, 143–151. doi:10.1002/jqs.2850
- 600 Cockcroft, M.J., Wilkinson, M.J., Tyson, P.D., 1987. The application of a present-day climatic model to  
601 the late Quaternary in southern Africa. *Clim. Chang.* 10, 161–181. doi:10.1007/BF00140253
- 602 Cohen, A., Tyson, P.D., 1995. Sea-surface temperature fluctuations during the Holocene off the  
603 south coast of Africa: implications for terrestrial climate and rainfall. *The Holocene* 5, 304–312.  
604 doi:10.1177/095968369500500305
- 605 Deacon, H.J., Geleijnse, V.B., 1988. The stratigraphy and sedimentology of the main site sequence,  
606 Klasies River, South Africa. *South African Archaeol. Bull.* 43, 5–14. doi:10.2307/3887608
- 607 Deacon, J., 1986. *The Later Stone Age of Southernmost Africa*. University of Cape Town.
- 608 Ferguson, J.E., Henderson, G.M., Fa, D.A., Finlayson, J.C., Charnley, N.R., 2011. Increased seasonality  
609 in the Western Mediterranean during the last glacial from limpet shell geochemistry. *Earth*  
610 *Planet. Sci. Lett.* 308, 325–333. doi:10.1016/j.epsl.2011.05.054
- 611 Fischer, H., Fundel, F., Ruth, U., Twarloh, B., Wegner, A., Udisti, R., Becagli, S., Castellano, E.,  
612 Morganti, A., Severi, M., Wolff, E., Littot, G., Röthlisberger, R., Mulvaney, R., Hutterli, M.A.,  
613 Kaufmann, P., Federer, U., Lambert, F., Bigler, M., Hansson, M., Jonsell, U., Angelis, M. de,  
614 Boutron, C., Siggaard-Andersen, M.-L., Steffensen, J.P., Barbante, C., Gaspari, V., 2007.  
615 Reconstruction of millennial changes in dust emission, transport and regional sea ice coverage  
616 using the deep EPICA ice cores from the Atlantic and Indian Ocean sector of Antarctica. *Earth*  
617 *Planet. Sci. Lett.* 260, 340–354. doi:10.1016/j.epsl.2007.06.014
- 618 Fisher, E.C., Akkaynak, D., Harris, J., Herries, A.I.R., Jacobs, Z., Karkanis, P., Marean, C.W., McGrath,  
619 J.R., 2015. Technical considerations and methodology for creating high-resolution, color-

- 620 corrected, and georectified photomosaics of stratigraphic sections at archaeological sites. *J.*  
621 *Archaeol. Sci.* 57, 380–394. doi:10.1016/j.jas.2015.02.022
- 622 Foster, G., 1997. Growth, reproduction and feeding biology of *Turbo sarmaticus* (Mollusca:  
623 Vetigastropoda) along the coast of the Eastern Cape Province of South Africa. Rhodes  
624 University.
- 625 Foster, G., Hodgson, A., Balarin, M., 1999. Effect of diet on growth rate and reproductive fitness of  
626 *Turbo sarmaticus* (Mollusca: Vetigastropoda: Turbinidae). *Mar. Biol.* 134, 307–315.  
627 doi:10.1007/s002270050548
- 628 Füllenbach, C.S., Schöne, B.R., Mertz-Kraus, R., 2015. Strontium/lithium ratio in aragonitic shells of  
629 *Cerastoderma edule* (Bivalvia)—A new potential temperature proxy for brackish environments.  
630 *Chem. Geol.* 417, 341–355.
- 631 Galimberti, M., 2010. Investigating the use of oxygen and carbon isotopes and sclerochronology on  
632 *Turbo sarmaticus* and *Donax serra* for palaeoenvironment reconstruction at Pinnacle Point,  
633 South Africa. University of Cape Town.
- 634 Galimberti, M., Loftus, E., Sealy, J.C., 2016. Investigating  $\delta^{18}\text{O}$  of *Turbo sarmaticus* (L. 1758) as an  
635 indicator of sea surface temperatures. *Palaeogeogr. Palaeoclimatol. Palaeoecol.* in press.
- 636 Grossman, E., Ku, T., 1986. Oxygen and carbon isotope fractionation in biogenic aragonite:  
637 temperature effects. *Chem. Geol. Isot. Geosci. Sect.* 59, 59–74. doi:10.1016/0168-  
638 9622(86)90057-6
- 639 Henshilwood, C.S., 2008. Holocene prehistory of the southern Cape. Excavations at Blombos Cave  
640 and Blombosfontein Nature Reserve. BAR International Series 1860. Cambridge Monographs in  
641 African Archaeology, 75, Cambridge.
- 642 Holmgren, K., Lee-Thorp, J.A., Cooper, G.R.J., Lundblad, K., Partridge, T.C., Scott, L., Sithaldeen, R.,  
643 Talma, S.A., Tyson, P.D., 2003. Persistent millennial-scale climatic variability over the past  
644 25,000 years in Southern Africa. *Quat. Sci. Rev.* 22, 2311–2326. doi:10.1016/S0277-  
645 3791(03)00204-X
- 646 Hudson, J.D., Anderson, T.F., 1989. Ocean temperatures and isotopic compositions through time.  
647 *Trans. R. Soc. Edinb. Earth Sci.* 80, 183–192. doi:10.1017/S0263593300028625
- 648 Karkanas, P., Brown, K.S., Fisher, E.C., Jacobs, Z., Marean, C.W., 2015. Interpreting human behavior  
649 from depositional rates and combustion features through the study of sedimentary microfacies  
650 at site Pinnacle Point 5-6, South Africa. *J. Hum. Evol.* 85, 1–21.  
651 doi:10.1016/j.jhevol.2015.04.006
- 652 Kim, S.-T., Mucci, A., Taylor, B., 2007. Phosphoric acid fractionation factors for calcite and aragonite  
653 between 25 and 75 °C: Revisited. *Chem. Geol. Isot. Geosci.* 246, 135–146.
- 654 Kyriacou, K., 2009. The reinvestigation of Hoffman's/Robberg Cave - the artefactual and shellfish  
655 assemblages. University of Cape Town.
- 656 Langejans, G.H.J., Niekerk, K. van, Dusseldorp, G.L., Thackeray, J.F., 2012. Middle Stone Age shellfish  
657 exploitation: Potential indications for mass collecting and resource intensification at Blombos  
658 Cave and Klasies River, South Africa. *Quat. Int.* 270, 80–94. doi:10.1016/0168-9622(86)90057-6
- 659 Lee-Thorp, J.A., Holmgren, K., Lauritzen, S.E., Linge, H., Moberg, A., Partridge, T.C., Stevenson, C.,  
660 Tyson, P.D., 2001. Rapid climate shifts in the southern African interior throughout the mid to  
661 late Holocene. *Geophys. Res. Lett.* 28, 4507–4510. doi:10.1029/2000GL012728
- 662 Loftus, E., Rogers, K., Lee-Thorp, J.A., 2015. A simple method to establish calcite:aragonite ratios in

- 663 archaeological mollusc shells. *J. Quat. Sci.* 30, 731–735. doi:10.1002/jqs.2819
- 664 Loftus, E., Sealy, J.C., Lee-Thorp, J.A., 2016. New Radiocarbon Dates and Bayesian Models for Nelson  
665 Bay Cave and Byneskranskop 1: Implications for the South African Later Stone Age Sequence.  
666 *Radiocarbon* 58, 365–381. doi:10.1017/RDC.2016.12
- 667 Partridge, T.C., Demenocal, P.B., Lorentz, S.A., Paiker, M., Vogel, J.C., 1997. Orbital forcing of climate  
668 over South Africa: a 200,000-year rainfall record from the Pretoria Saltpan. *Quat. Sci. Rev.* 16,  
669 1125–1133.
- 670 Schumann, E., 1999. Wind-driven mixed layer and coastal upwelling processes off the south coast of  
671 South Africa. *J. Mar. Res.* 57, 671–691. doi:10.1357/002224099321549639
- 672 Schumann, E., Cohen, A., Jury, M.R., 1995. Coastal sea surface temperature variability along the  
673 south coast of South Africa and the relationship to regional and global climate. *J. Mar. Res.* 53,  
674 231–248. doi:10.1357/0022240953213205
- 675 Schweitzer, F.R., Wilson, M., 1982. Byneskranskop 1: A Late Quaternary living site in the southern  
676 Cape Province. *Ann. South African Museum* 88, 1–102.
- 677 Scott, L., Lee-Thorp, J.A., 2004. Holocene climatic trends and rhythms in Southern Africa, in:  
678 Battarbee, R.W., Gasse, F., Stickley, C.E. (Eds.), *Past Climate Variability through Europe and*  
679 *Africa*. Springer Netherlands, Amsterdam, pp. 69–91.
- 680 Scott, L., Neumann, F.H., Brook, G.A., Bousman, C.B., Norström, E., Metwally, A.A., 2012. Terrestrial  
681 fossil-pollen evidence of climate change during the last 26 thousand years in Southern Africa.  
682 *Quat. Sci. Rev.* 32, 100–118. doi:10.1016/j.quascirev.2011.11.010
- 683 Scott, L., Nyakale, M., 2002. Pollen indications of Holocene palaeoenvironments at Florisbad in the  
684 Central Free State, South Africa. *The Holocene* 14, 497–503. doi:10.1191/0959683602hl563rr
- 685 Shackleton, N., 1982. Stratigraphy and chronology of the KRM deposits: oxygen isotope evidence.,  
686 in: Singer, R., Wymer, J.J. (Eds.), *The Middle Stone Age at Klasies River Mouth in South Africa*.  
687 University of Chicago, Chicago, pp. 192–199.
- 688 Simon, M.H., Arthur, K.L., Hall, I.R., Peeters, F.J.C., Loveday, B.R., Barker, S., Ziegler, M., Zahn, R.,  
689 2013. Millennial-scale Agulhas Current variability and its implications for salt-leakage through  
690 the Indian-Atlantic Ocean Gateway. *Earth Planet. Sci. Lett.* 383, 101–112.  
691 doi:10.1016/j.epsl.2013.09.035
- 692 Tyson, P.D., Preston-Whyte, R., 2000. *The weather and climate of southern Africa*. Oxford University  
693 Press, Cape Town.
- 694 Urey, H., Lowenstam, H.A., Epstein, S., McKinney, C.R., 1951. Measurement of paleotemperatures  
695 and temperatures of the Upper Cretaceous of England, Denmark, and the southeastern United  
696 States. *Geol. Soc. Am. Bull.* 62, 399. doi:10.1130/0016-7606(1951)62[399:MOPATO]2.0.CO;2
- 697 van Andel, T.H., 1989. Late Pleistocene Sea Levels and the Human Exploitation of the Shore and Shelf  
698 of Southern South Africa. *J. F. Archaeol.* 16, 133–155. doi:10.1179/jfa.1989.16.2.133
- 699 Waelbroeck, C., Labeyrie, L., Michel, E., Duplessy, J.C., McManus, J.F., Lambeck, K., Balbon, E.,  
700 Labracherie, M., 2002. Sea-level and deep water temperature changes derived from benthic  
701 foraminifera isotopic records. *Quat. Sci. Rev.* 21, 295–305. doi:10.1016/S0277-3791(01)00101-9
- 702 Wurz, S., 2002. Variability in the middle stone age lithic sequence, 115,000-60,000 years ago at  
703 Klasies river, South Africa. *J. Archaeol. Sci.* 29, 1001–1015. doi:10.1006/jasc.2001.0799
- 704 Ziegler, M., Simon, M., Hall, I., Barker, S., Stringer, C.B., Zahn, R., 2013. Development of Middle Stone

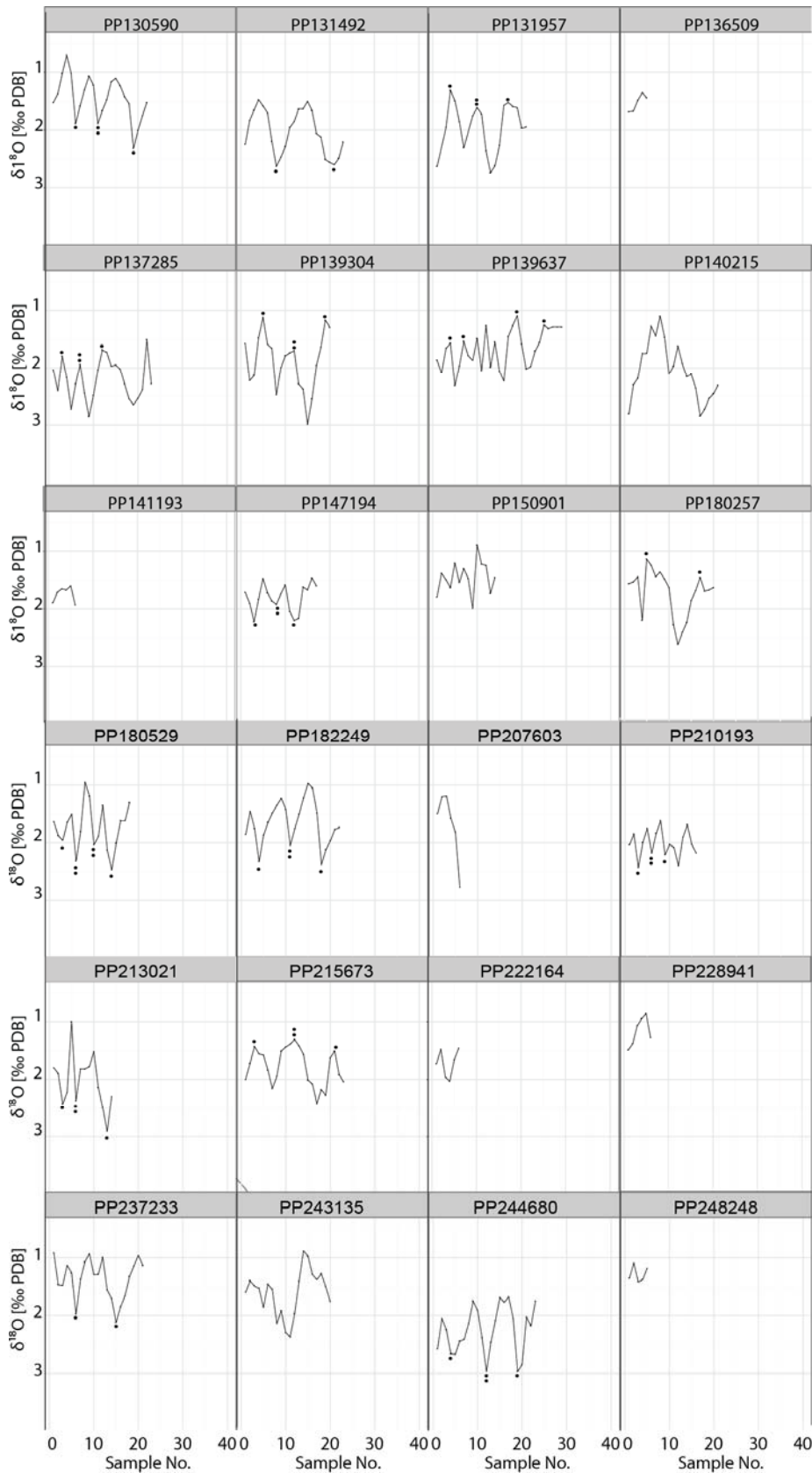
705 Age innovation linked to rapid climate change. Nat. Commun. 4, 1905.  
706 doi:10.1038/ncomms2897  
707



709

710 **SM Figure 1** Serial  $\delta^{18}\text{O}$  sequences from twenty-seven Holocene and Pleistocene aged *Turbo*  
 711 *sarmaticus* opercula (see Table 1 for context).



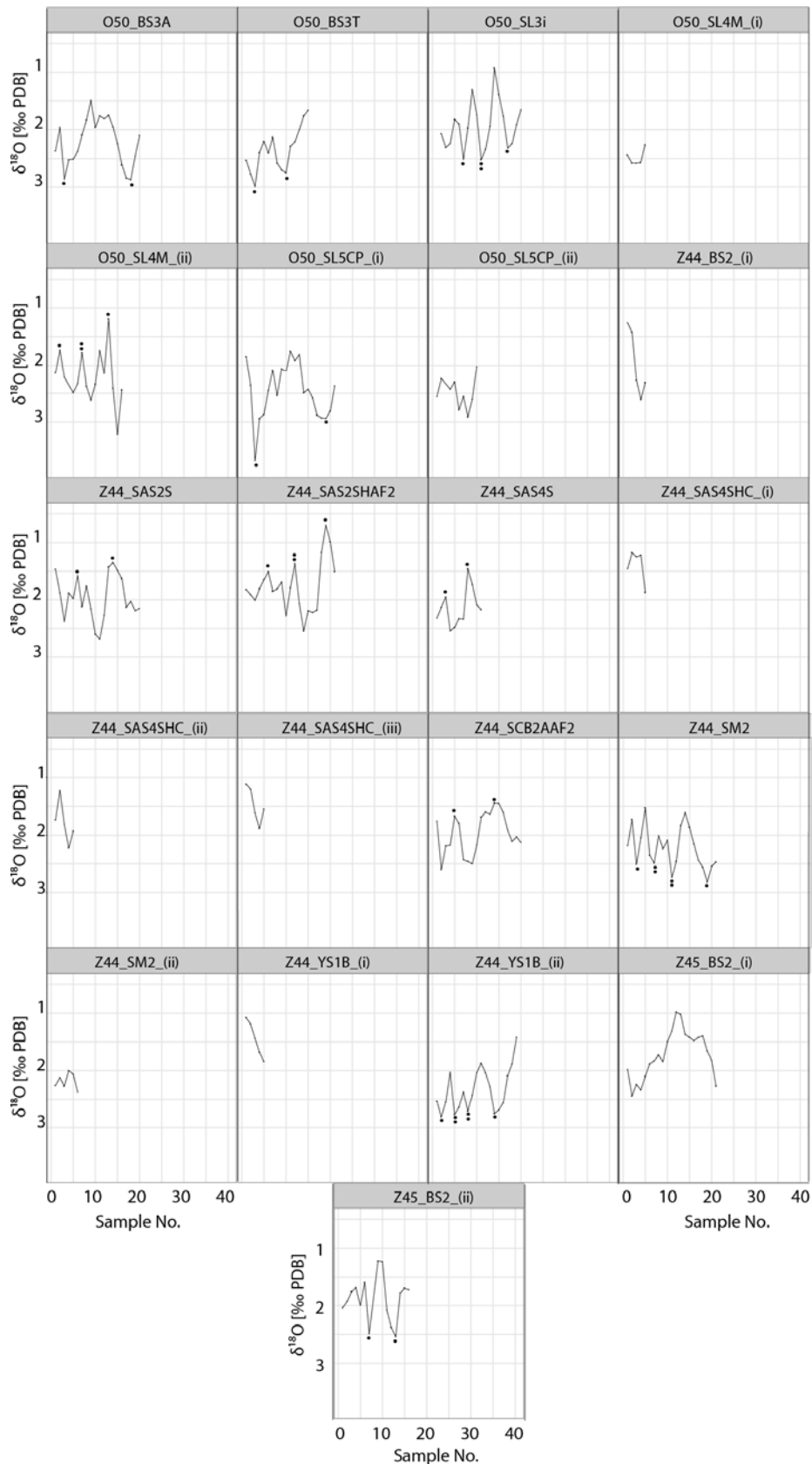


712

713 **SM Figure 2** Serial  $\delta^{18}\text{O}$  sequences from twenty-four *Turbo sarmaticus* opercula from Pinnacle Point  
 714 5-6 (see Table 1 for context of each shell).

715

716



717

718 **SM Figure 3** Serial  $\delta^{18}\text{O}$  sequences from twenty-one *Turbo sarmaticus* opercula from Klasies River  
 719 main site (see Table 1 for context of each shell).